ATLAS NOTE

ATLAS-CONF-2011-123

August 30, 2011

A Search for $t\bar{t}$ Resonances in the Dilepton Channel in 1.04 fb^{-1} of pp collisions at $\sqrt{s} = 7$ TeV with the ATLAS experiment

The ATLAS collaboration

Abstract

This note presents a search for a high mass $t\bar{t}$ resonance in pp collisions at $\sqrt{s} = 7$ TeV at the LHC. We search for such a resonance using the final state where the W bosons from the top quark decay into either an electron and electron-neutrino or a muon and muon-neutrino (dilepton final state). The data were recorded by the ATLAS experiment during 2011 and correspond to a total integrated luminosity of $\mathcal{L}$=1.04 fb^{-1}. No statistically significant excess above the Standard Model expectation is observed. Upper limits at the 95% Confidence Level are set on the cross section times branching ratio of the resonance decaying to $t\bar{t}$ pairs as a function of the resonance mass. A lower mass limit of 0.84 TeV is set for the case of a Kaluza-Klein gluon resonance in the Randall-Sundrum Model.

1 Introduction

Many models of physics beyond the Standard Model (BSM) predict the existence of new resonances that decay predominantly into top quark pairs. The top quark is unique among the known matter constituents. It is the only fermion whose mass is very close to the scale of electroweak symmetry breaking. Partly due to this reason, the top quark has a special treatment in many BSM scenarios. These include alternative mechanisms of electroweak symmetry breaking (Topcolor, top see-saw)[1] as well as models that aim at the stabilization of the Higgs mass (supersymmetry, extra dimensions). In many such models gauge interactions exist whose coupling to the third generation quarks, and in particular to the top quark, are enhanced [2]. These include Kaluza-Klein (KK) excitations of the graviton, gluon as well as other gauge bosons which couple to top quarks [3][4].

This note provides a description of the ATLAS search for new heavy particles decaying to $t\bar{t}$ pairs in the dilepton channel. Three final state topologies are considered: dimuon, dielectron and electron-muon, resulting from the leptonic decays of the two W bosons from the top quark decay. Despite the lower branching ratio of the dilepton channel compared to lepton+jets, the dilepton channel has a cleaner final state and hence is less sensitive to Monte Carlo modeling problems of non-top background. Furthermore this channel will be invaluable to confirm and characterize the nature of a potential new signal in other channels.

Two variables of particular interest in this analysis are H_T and E_T^{miss}. H_T is defined as the scalar sum of the transverse momenta of the two identified leptons and all the jets in the event above a given momentum threshold. E_T^{miss} is the missing transverse momentum from the escaping neutrinos from the leptonic W boson decay. This analysis searches for an excess in the $H_T + E_T^{miss}$ spectrum. The $H_T + E_T^{miss}$ distribution of a heavy KK-gluon resonance will be harder than that for Standard Model top quark production.

In the absence of any significant signal, limits on the production cross section times branching ratio (σB) are set for a series of resonance masses using a template shape fitting method. The limits on σB are translated into limits on the resonance mass using predictions for a Kaluza-Klein gluon resonance in the Randall-Sundrum Model. While our benchmark model is the KK-gluon in the Randall-Sundrum model, this search is also sensitive to other resonances decaying to top quark pairs.

Although this is the first result obtained in the dilepton channel, previous results obtained in the lepton+jets channel exist from the ATLAS [5], CMS [6], CDF [7] and DØ [8] collaborations.

2 ATLAS detector

The three main detector systems of ATLAS [9] used in this analysis are the inner tracking detector, the calorimeter, and the muon spectrometer. Charged particle tracks and vertices are reconstructed with the inner detector (ID) which consists of silicon pixel, silicon strip, and transition radiation detectors covering the pseudorapidity range $|\eta| < 2.5$ [1]. It is immersed in a 2 T magnetic field provided by a superconducting solenoid. The latter is surrounded by a finely-segmented, hermetic sampling calorimeter that covers $|\eta| < 4.9$ and provides three-dimensional reconstruction of particle showers. The electromagnetic compartment of the calorimeter uses lead and liquid argon in the region up to $|\eta| < 3.2$. The hadronic compartment is based on iron and scintillator tiles in the region up to $|\eta| < 1.7$ and copper and liquid argon in the region $1.5 < |\eta| < 3.2$. The forward calorimeter covers the region $3.1 < |\eta| < 4.9$; the first layer is copper and liquid argon and the second and third layers are tungsten and liquid argon. Outside

---

[1] ATLAS uses a right-handed coordinate system with its origin at the nominal interaction point (IP) in the centre of the detector and the z-axis along the beam pipe. The x-axis points from the IP to the centre of the LHC ring, and the y axis points upward. Cylindrical coordinates (r, ϕ) are used in the transverse plane, ϕ being the azimuthal angle around the beam pipe. The pseudorapidity is defined in terms of the polar angle θ as $\eta = -\ln\tan(\theta/2)$.

the calorimeter, there is a muon spectrometer with air-core toroids providing a magnetic field. Three sets of drift tubes or cathode strip chambers provide precision (η) coordinates for momentum measurement in the region $|\eta| < 2.7$. Finally, resistive-plate and thin-gap chambers provide muon triggering capability up to $|\eta| < 2.4$.

3 Event simulation

Monte Carlo (MC) samples with full ATLAS detector simulation [10] based on the Geant4 program [11] are used to model the signal process and most of the backgrounds. The signal process is generated using the Madgraph [12] and Pythia programs [13]. The primary background in the high $H_T + E_T^{miss}$ region comes from direct Standard Model $t\overline{t}$ production. To simulate this background, we use the MC@NLO [14] generator with the CTEQ6.6 [15] parton distribution function. The parton shower and the underlying event were added using the Herwig [16] generator and Jimmy [17] underlying event model. The $t\overline{t}$ cross section is normalized to the approximate next-to-next-to leading order prediction value of 164.6 pb, obtained using the Hathor tool [18].

Other backgrounds considered are those arising from Z + jets production with the Z boson decaying to dileptons as well as diboson production. These backgrounds were simulated using Alpgen [19] interfaced to the Herwig generator and Jimmy underlying event model.

QCD multijet production, and the W+jets process in which a jet is misidentified as a lepton also contribute to the background and are estimated and modeled using data.

4 Object Definition and Event selection

The data analyzed were collected in the period from March to July 2011, corresponding to a total integrated luminosity of $\mathcal{L}$=1.04 fb^{-1}[20]. The selection of $t\overline{t}$ events makes use of reconstructed electrons, muons, jets and E_T^{miss}. The following criteria are used to define the selected objects in the events.

Events in each channel must satisfy good data quality requirements, i.e. proper functioning of the ID, solenoid, calorimeter and trigger subsystems, as well as the presence of stable beams from the LHC. We require the events to have been triggered by either a single-electron trigger with a transverse energy threshold of $E_T > 20$ GeV or a single-muon trigger with a transverse momentum threshold of $p_{\mathrm{T}} >$ 18 GeV.

Electron candidates are required to have transverse energy $E_T > 25$ GeV and $|\eta| < 2.47$. The region $1.37 \leq |\eta| \leq 1.52$ is excluded because it corresponds to a transition region between the barrel and endcap calorimeters that has a degraded energy resolution. The candidates are formed from clusters of cells reconstructed in the electromagnetic calorimeter. Candidate electrons are required to satisfy the *tight* electron definition [21], which involves criteria on the transverse shower shape, the longitudinal leakage into the hadronic calorimeter, and the association to an ID track. The electron energy is obtained from the calorimeter measurements and its direction from the associated track.

Muon tracks are reconstructed independently in both the inner detector and muon spectrometer, and their momenta are determined from a combined fit to the measurements from both sub-systems. The combined track is required to have a transverse momentum larger than 20 GeV with $|\eta| < 2.5$.

To reduce background from misreconstructed hadrons, photon conversions and semileptonic decays inside jets, the leptons in each event are required to be 'isolated' within a cone in $\eta - \phi$ space of radius $\Delta R = \sqrt{\Delta\eta^2 + \Delta\phi^2}$. For electrons, the calorimeter isolation transverse energy in a cone of $\Delta R = 0.2$ about the electron direction, corrected for electron leakage and for the dependence on the number of primary vertices, is required to be less than 3.5 GeV. For muons, the corresponding calorimeter isolation energy in a cone of $\Delta R = 0.3$ is required to be less than 4 GeV, and the analogous sum of track transverse momenta in a cone of $\Delta R = 0.3$ is also required to be less than 4 GeV. Muons are required to have a distance ΔR greater than 0.4 from any jet with $p_{\mathrm{T}} > 20$ GeV.

Each pair of muons passing these cuts are further checked against simple cosmic-muon rejection criteria. Events are removed if any combination has oppositely-signed impact parameters d_0, both muons fulfill $|d_0| > 0.5$ mm and if the muons are back-to-back, i.e. $\Delta\phi > 3.1$ between the two muon directions.

Jets are reconstructed with the anti-k_t algorithm ($R = 0.4$) [22] using noise-suppressed clusters as inputs, which helps reduce the contribution of electronic noise and activity from extra events (pileup) in the calorimeter. These jets are then calibrated to the hadronic energy scale [23], using p_{T} and η dependent correction factors obtained from simulation. The jet position is corrected to the primary vertex.

If a jet is the closest jet to an electron candidate and the corresponding distance ΔR between the jet and the calorimeter cluster of the electron is less than 0.2, the jet is removed from consideration in order to avoid double-counting of electrons as jets. Finally, only jets with $p_{\mathrm{T}} > 25$ GeV and $|\eta| < 2.5$ are considered. No explicit b-tagging of jets is required in this analysis.

The missing transverse momentum (E_T^{miss}) is constructed from the vector sum of the energies in all calorimeter cells associated to clusters, resolved into the transverse plane. Cells not associated with identified muons, electrons and photons (with $p_{\mathrm{T}} > 10$ GeV), taus, jets and soft jets are included at the electromagnetic scale.

To ensure that the event was actually triggered by the leptons used in the analysis at least one match between the reconstructed leptons and the trigger objects is required. For the matching the distance requirement is $\Delta R < 0.15$.

After the trigger selections, events must have an offline-reconstructed primary vertex with at least five tracks. Events in data are discarded if any jet with $p_T > 25$ GeV fails jet quality cuts designed to reject jets arising from out-of-time activity or calorimeter noise (jet cleaning cuts).

Candidate events are required to have two or more selected jets and exactly two oppositely-signed selected leptons. In order to suppress the Z+jets background, ee and $\mu\mu$ events are required to have an invariant dilepton mass ($m_{\ell\ell}$) outside the Z window, defined as $|m_Z - m_{\ell\ell}| < 10$ GeV, and $E_T^{miss} > 40$ GeV. An additional cut of $m_{\ell\ell} > 10$ GeV is applied to the data in order to conform with the lower $m_{\ell\ell}$ cut-off in the Z+jets Monte Carlo and to reduce backgrounds from meson resonances. In the $e\mu$ channel the non-$t\bar{t}$ background is suppressed by requiring $H_T > 130$ GeV.

5 Backgrounds

Apart from the dominant Standard Model $t\bar{t}$ background, there are three other categories of background sources. The second largest background originates from Drell-Yan processes ($Z/\gamma^* \to \ell^+\ell^-$) produced in association with jets, where the large E_T^{miss} arises due to resolution effects and measurement errors. $Z/\gamma^* \to \ell^+\ell^-$ (with $\ell = e, \mu$) is the second largest background source for the same-flavor channel analyses, while $Z/\gamma^* \to \tau^+\tau^-$ is the second largest background source for the $e\mu$ channel analysis. The size of the Drell-Yan backgrounds ($Z/\gamma^* \to e^+e^-, \mu^+\mu^-$) and the distributions for the misidentified primary lepton backgrounds are determined using data. The event selection includes cuts to reject Drell-Yan events. However, a small fraction of events in the E_T^{miss} tails and dilepton invariant mass sidebands will be selected by the signal selection. To estimate the Drell-Yan background (excluding the decay to $\tau^+\tau^-$) in the tail region, the number of Drell-Yan events is measured in a control region orthogonal to the signal region. The control region consists of events with at least two jets, an invariant dilepton mass inside the 'Z-window', and with $E_T^{miss} > 40$ GeV; a wider Z-window is used for events with $E_T^{miss} > 20$ GeV and $E_T^{miss} \leq 40$ GeV.

The contamination in the control region from background physics processes and its contribution is subtracted from data relying on the Monte Carlo prediction. A scale factor is derived using Drell-Yan simulations to extrapolate from the control region (CR) into the signal region (SR):

$$\text{Drell}-\text{Yan background estimates} = \frac{\text{MC}_{\text{Drell-Yan}}(\text{SR})}{\text{MC}_{\text{Drell-Yan}}(\text{CR})} \times (\text{Data(CR)} - \text{MC}_{\text{other}}(\text{CR})) \quad (1)$$

where $\text{MC}_{\text{Drell-Yan}}(\text{SR}/\text{CR})$ represent the number of events in the signal and control region, respectively. MC_{other} is the number of events from physics backgrounds that contaminate the control region. Data(CR) is the observed number of events in the control region in data. The Drell-Yan background normalization prediction from the Monte Carlo is thus scaled by the ratio of data and Monte Carlo events in the control region. This scale factor is close to unity in both channels, 1.02 ± 0.03 in the electron and 1.04 ± 0.02 in the muon channel, where the quoted uncertainties are statistical only.

Another source of background events is from processes that contain misidentified hadrons or semileptonic decays inside jets (fakes). These are W boson events, produced in association with jets, and QCD multi-jet events. The contribution of these events is estimated from data using the Matrix Method [24] which accounts intrinsically for backgrounds with one and two fake leptons. We assign a 50% systematic uncertainty to the fake background estimate derived from the uncertainty on the misidentification rates. We also evaluate the effect of systematic uncertainty in the fake background on the shape of the $H_T + E_T^{miss}$ distribution.

The remaining background sources are electroweak processes including two leptons in the decay such as Wt and diboson (WW, ZZ and WZ) production processes. The contributions from these sources are small and they are determined from Monte Carlo simulations.

The background predictions in the signal region from the different sources are listed in Table 1. The Monte Carlo is normalized using the ATLAS luminosity measurement.

Table 1: Background composition in the signal region. Both statistical and systematic uncertainties are included.

Process	Predicted number of background events
$t\bar{t}$	1920^{+230}_{-220}
$Z/\gamma^* \to ee$ + jets	130^{+72}_{-49}
$Z/\gamma^* \to \mu\mu$ + jets	140^{+27}_{-21}
$Z/\gamma^* \to \tau\tau$ + jets	85^{+12}_{-10}
Diboson	83^{+13}_{-12}
Single top	98^{+14}_{-13}
Fakes	96^{+94}_{-51}
Total background	2550^{+330}_{-300}
Data	2659

Figures 1 and 2 show data-Monte Carlo comparisons for relevant quantities that enter into the $H_T + E_T^{miss}$ calculation. The discontinuity in the E_T^{miss} distribution in Figure 2 is due to the cut on H_T, instead of on E_T^{miss}, in the $e\mu$ channel. The hashed band corresponds to the Monte Carlo statistical and systematic uncertainty.

6 Systematic Uncertainties

This analysis requires input from theoretical models, Monte Carlo simulations, and extrapolations from control samples in data. We assign systematic uncertainties to our predictions and include the effects of these uncertainties on the measured cross section and mass limits.

Two categories of systematic uncertainty were considered: uncertainty in the predicted rates of the signal and background processes and uncertainty in the shape of the $H_T + E_T^{miss}$ distribution. A given systematic uncertainty may affect multiple signal and background components. The effects of systematic

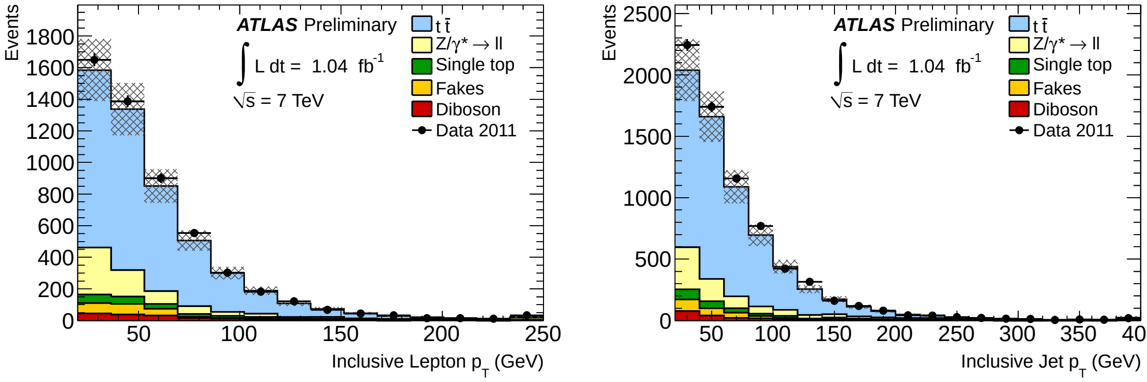

Figure 1: Data-Monte Carlo comparison of the transverse momentum of both leptons in the event (left) and all jets in the event (right). The points represent ATLAS data and the filled histograms show the simulated backgrounds including the statistical and systematic uncertainty represented by the hashed band.

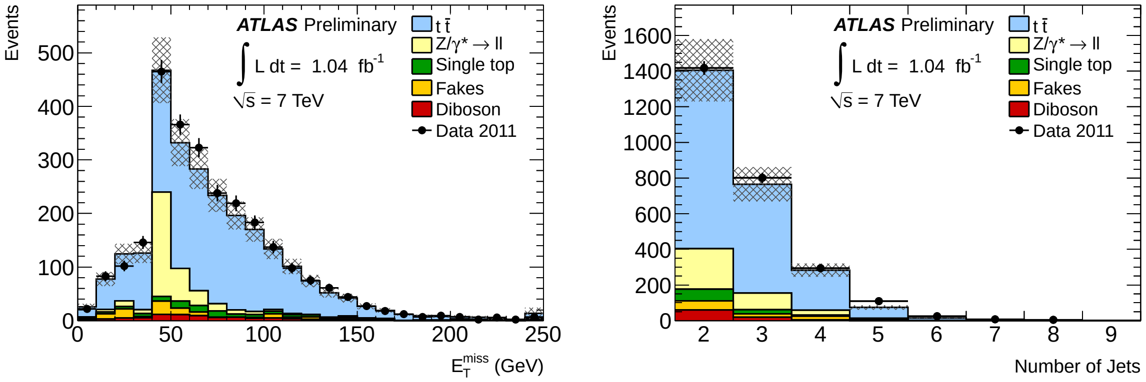

Figure 2: Data-Monte Carlo comparison of the missing transverse momentum in the event (left) and number of selected jets in the event (right). The points represent ATLAS data and the filled histograms show the simulated backgrounds including the statistical and systematic uncertainty represented by the hashed band.

uncertainties from the same source are considered to be fully correlated. For example, the jet energy scale (JES) uncertainty affects the predictions of the Monte Carlo based background processes as well as the signal, so the uncertainty on the JES affects all processes in a correlated way. The effects of different sources of systematic uncertainty are considered to be uncorrelated.

The rate uncertainties were quantified by evaluating the relative change in total acceptance for signal and background Monte Carlo samples after applying $\pm 1\sigma$ shifts (where appropriate) due to each source of systematic uncertainty. Shape uncertainties on the $H_T + E_T^{miss}$ distribution are estimated comparing the bin-by-bin relative variations from the nominal normalized distributions.

The following sources of systematic uncertainties were evaluated:

- Reconstruction, identification and trigger efficiencies.
- Jet energy scale. The jet energy scale was derived using information from test-beam data, LHC collision data and simulation. Its uncertainty varies between 2.5% and 8% (3.5% and 14%) in the central (forward) region, depending on jet p_T and η [23]. This includes uncertainties in the flavor

composition of the samples and mis-measurements from close-by jets. Additional uncertainties due to pileup can be as large as 5% (7%) in the central (forward) region.

- Jet energy resolution. The energy resolution of jets was measured in dijet events and agrees with predictions from simulations within 10%.
- Initial and final state radiation (ISR/FSR). Dedicated $t\bar{t}$ samples produced with increased and decreased amounts of QCD radiation were compared to a nominal sample. The amount of initial and final state radiation was varied by modifying parameters in ACERMC [25] interfaced to PYTHIA. The parameters were varied in a range comparable to those used in the Perugia Soft/Hard tune variations [26]. This uncertainty is extrapolated to the signal by separating the Standard Model samples into bins of different $t\bar{t}$ invariant mass.
- Parton Shower. To evaluate the systematic uncertainty due to the parton shower model for $t\bar{t}$ production, we compare two PowHeg [27] samples interfaced to HERWIG and PYTHIA, respectively.
- Generator uncertainty. The uncertainty due to generator dependence for $t\bar{t}$ production is estimated by comparing $t\bar{t}$ events generated with PowHeg interfaced with Herwig to the default sample generated with MC@NLO and Pythia.
- PDF uncertainty. The PDF uncertainties are evaluated with three PDF sets, namely CTEQ6.6[28], MSTW2008NLO (68% C.L.)[29] and NNPDF2.0. For each PDF error set, the $H_T + E_T^{miss}$ distribution is recomputed. We assign the envelope from all three variations to be the PDF uncertainty [24]. For the signal samples solely the change resulting from the modification of the acceptance is used as the systematic error.

The following global systematic uncertainties are considered:

- The uncertainty on the luminosity determination is 3.7 % [20]. This is applied to both signal and background processes.
- Background cross sections. All background cross sections are varied within their theoretical uncertainty. These are ±9% for $t\bar{t}$, ±10% for single top and ±5% for the diboson samples. For Z + jets the uncertainty in the data driven normalization is used.

The following systematic uncertainties were also considered and were found to have a negligible effect: jet reconstruction efficiency, lepton energy scale and resolution, the contribution of calorimeter clusters not associated to any final state object in the E_T^{miss} calculation. Table 2 summarizes the acceptance change due to different systematic uncertainties.

7 Statistical Analysis

Template shape fitting is employed to test the consistency of the Standard Model background hypothesis with the observed data over the spectrum of the $H_T + E_T^{miss}$ distribution.

Template shape fitting is essentially a counting experiment in many bins of the $H_T + E_T^{miss}$ distribution and the likelihood function is the product of single bin counting experiment likelihood functions. The sensitivity of the search is enhanced over a single bin counting experiment by the exclusive treatment of bins with different signal/background ratios. The shape information helps to better constrain the signal and background contribution of the candidate sample.

The expected number of events in bin k is represented by the Poisson mean μ_k, which is a sum of KK-gluon signal and total background ($N_{bkg} = N_{t\bar{t}} + N_{Z\text{+jets}} + N_{\text{Diboson}} + N_{\text{Singletop}} + N_{\text{Fakes}}$). The binned

Table 2: Change in acceptance due to various sources of systematic uncertainties. Positive and negative acceptance variations are listed in [%]. All signal systematic uncertainties have been symmetrized. The total systematic uncertainty for Standard Model background also includes luminosity (3.7%) and the cross-section uncertainties.

	SM background		m_{KK}=700 GeV	m_{KK}=1000 GeV
	(+)	(-)		
Lepton ID / Trigger	3.4	4.5	4.2	4.7
Jet energy scale	7.4	6.7	3.5	4.0
Jet energy resolution	2.3	-	2.5	6.8
ISR/FSR	0	2.3	2.5	4.5
Parton Shower	1.4	1.4	-	-
Generator	4.8	4.8	-	-
PDF	2.7	2.7	1.2	1.2
Total Systematic	12.8	11.5	6.6	10.3

likelihood function is shown in Equation 2. Signal and total background correspond to template numbers $j = 1$ and $j = 2$ respectively, G is a unit width Gaussian prior for nuisance parameters θ_i that control systematic rate variations (δ_{ji}) as well as bin-by-bin systematic shape variations (ϵ_{jik}) of the (unit area) template shapes T_{jk} in the likelihood function.

$$\mathcal{L}(\text{data}|N_j, \theta_i) = \prod_{k=1}^{N_{bin}} \frac{\mu_k^{n_k} e^{-\mu_k}}{n_k!} \prod_{i=1}^{N_{sys}} G(\theta_i, 0, 1) \quad \text{, where } \mu_k = \sum_j N_j \underbrace{\prod_{i=1}^{N_{sys}} (1 + \theta_i \delta_{ji})}_{Rate\ Uncertainty} \underbrace{\prod_{i=1}^{N_{sys}} (1 + \theta_i \epsilon_{jik})}_{Shape\ Uncertainty} T_{jk} \tag{2}$$

For a fixed value of the resonance mass we perform a signal scan using the likelihood function of Equation 2.

Figure 15 shows the $H_T + E_T^{miss}$ distribution for data and all backgrounds together with a hypothetical KK-gluon signal with a mass of 700 GeV for illustration.

In order to test the signal hypothesis we evaluate a p-value for the data. The p-value quantifies, in the absence of signal, the probability of observing a resonant excess anywhere in the $H_T + E_T^{miss}$ distribution, with a significance at least as great as that observed in the data. Since the resulting p-value is 40%, no statistically significant excess above the predictions of the SM has been observed.

In the absence of a signal, we set 95% Confidence Level (C.L.) upper limits on the KK-gluon production cross section times branching ratio using a Bayesian approach. This is repeated for a sequence of resonance masses ranging from 500 – 1600 GeV.

The reduced likelihood, which is only a function of the parameter of interest ($N_{KK-gluon}$) is obtained by means of a marginalization technique using Markov Chain Monte Carlo as implemented in the Bayesian Analysis Toolkit [30].

$$\mathcal{L}'(\text{data}|N_{KK-gluon}) = \int \mathcal{L}(N_j, \theta_1, ..., \theta_N) d\theta_1, ..., d\theta_N \tag{3}$$

The reduced likelihood function is converted into a Bayesian posterior probability density using Bayes' theorem, assuming a uniform (non-informative) positive prior in (σB), i.e. $\pi(\sigma B) = 1$. The maximum of the posterior probability density $P(\sigma B|\text{data})$ corresponds to the most likely signal content given the data. The 95% Bayesian upper limit is obtained by integrating the posterior probability density.

The cross section limits are converted into mass limits using the theoretical (σB) dependence of the KK-gluon on the resonance mass. Our interpretation of this model does not consider any possible interference effects.

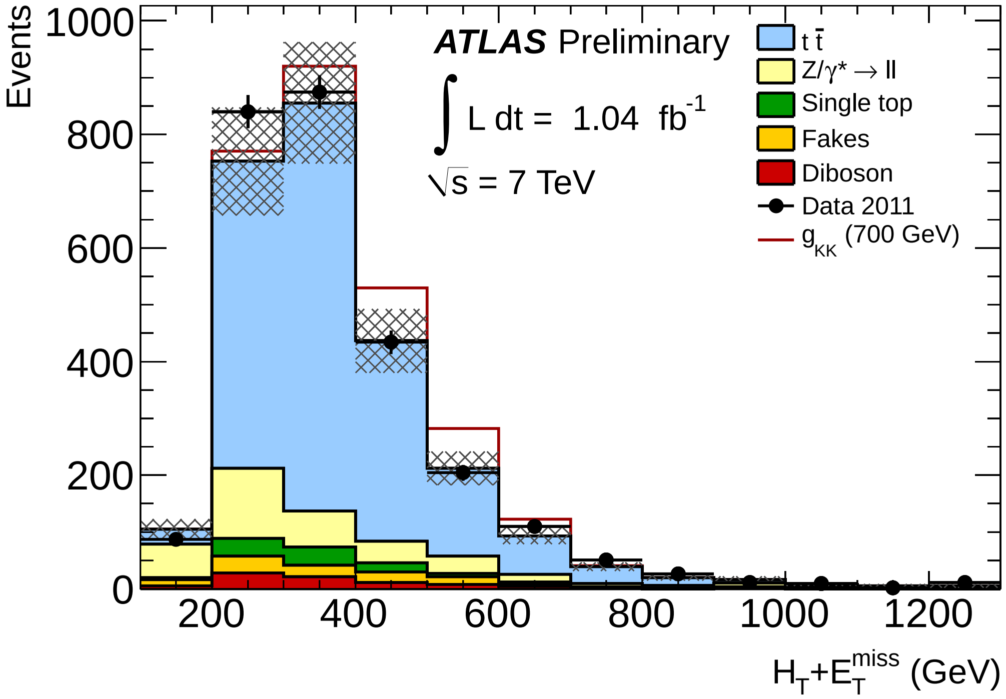

Figure 3: Data - Monte Carlo comparison for the $H_T + E_T^{miss}$ distribution together with a KK-gluon signal with a mass of 700 GeV for illustration. The statistical and systematic uncertainty on the Monte Carlo is represented by the hashed band.

To estimate the *a priori* sensitivity for this search Monte Carlo pseudo-experiments are generated using only Standard Model processes in proportion to their expected rate. The pseudo-experiments are randomly drawn from Monte Carlo samples of all relevant backgrounds. The nuisance parameters are allowed to randomly vary within their prior distributions for each pseudo-experiment. It was ensured that the sampling of the priors was not truncated in the analysis. The median of the distribution is chosen to represent the expected limit. The ensemble of limits is also used to find the 68% and 95% envelope of limits as a function of resonance mass.

Figure 4 shows the 95% C.L. exclusion limit on the cross section times branching ratio. The signal cross section for the KK-gluon production with subsequent decay to $t\bar{t}$ pairs is available in a recent version of Pythia [31] with input from [32] which has been used for this analysis. The coupling of light quarks to the KK-gluon is varied by scaling the strong coupling parameter $g_{qqg_{KK}}/g_s$ in a range from 0.2 to 0.35, where 0.2 corresponds to the default coupling in the Randall-Sundrum model, and the other couplings are within a reasonable range constrained by the uncertainty in the light quark masses[2]. Four cross section curves are calculated for four different couplings, each using the MRST 2007 LO* PDF [33]. Table 3 lists the expected and observed mass limits obtained for each model point.

8 Conclusions

The ATLAS detector has been used to search for high-mass resonances in the dilepton $t\bar{t}$ final state. The $H_T + E_T^{miss}$ observable is well described by the Standard Model backgrounds. We find no significant excess at high $H_T + E_T^{miss}$ in the data, and set limits on the cross section times branching ratio for

---

[2] The sign of $g_{qqg_{KK}}/g_s$ is negative, which is important if interference terms are taken into consideration.

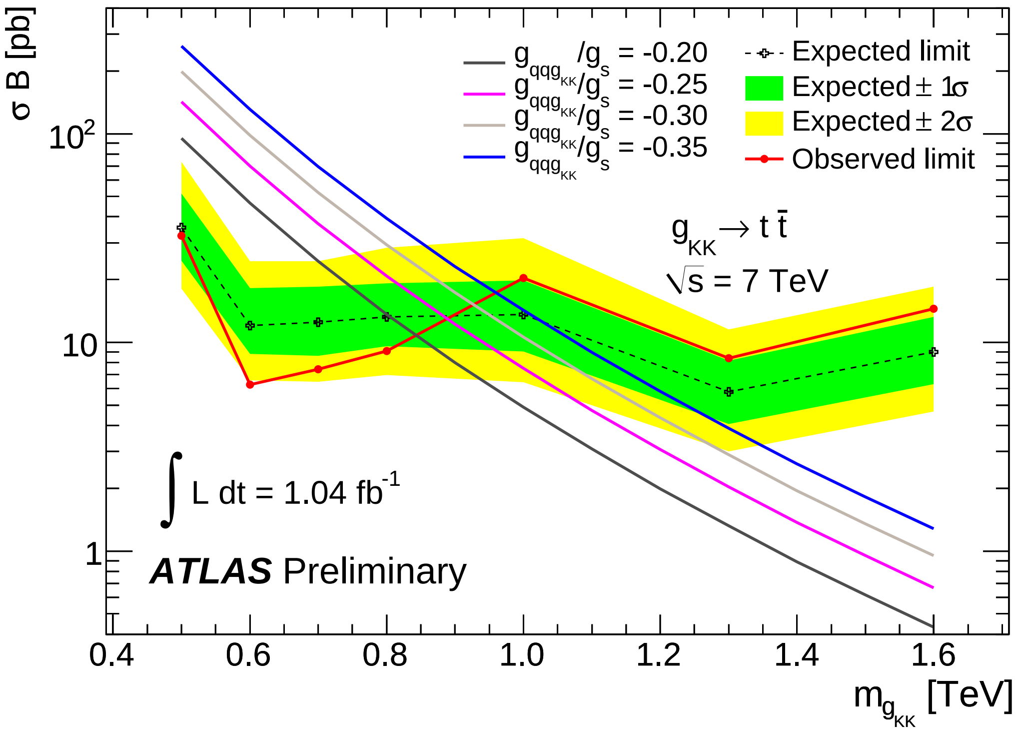

Figure 4: Expected and observed limits on cross section times branching ratio at 95% C.L. and expected cross section for a Randall-Sundrum KK-gluon g_{KK}. Cross sections were calculated using the MRST 2007 LO* PDF.

Table 3: Expected and observed lower limits on the KK-gluon mass in the Randall-Sundrum model

	Mass Limit (TeV)	
$g_{qqg_{KK}}/g_s$	Expected	Observed
-0.20	0.80	0.84
-0.25	0.88	0.88
-0.30	0.95	0.92
-0.35	1.02	0.96

KK-gluon production as well as upper limits at 95% C.L. on the mass of the KK-gluon in the Randall-Sundrum model of 0.84 TeV.

For resonance masses above approximately 1 TeV, the top quark decay products start to become strongly collimated. A search taking into account such final state topologies as well as reconstruction of the resonance mass is the subject of a forthcoming analysis.

References

[1] C. T. Hill and S. J. Parke, *Top quark production: Sensitivity to new physics*, Phys. Rev. **D49** (1994) 4454.

[2] R. Frederix and F. Maltoni, *Top pair invariant mass distribution: a window on new physics*, JHEP **0901** (2007) 047.

[3] K. Agashe et. al., *LHC Signals from Warped Extra Dimensions*, `arXiv:hep-ph/0612015`.

[4] B. L. et. al., *The Bulk RS KK-gluon at the LHC*, JHEP **09** (2007) 074.

[5] ATLAS Collaboration, *A Search for $t\bar{t}$ Resonances in the Lepton Plus Jets Channel using* 200 pb^{-1} *of pp Collisions at sqrt(s) = 7 TeV*, `https://atlas.web.cern.ch/Atlas/GROUPS/PHYSICS/CONFNOTES/ATLAS-CONF-2011-087`.

[6] CMS Collaboration, *Search for Resonances in Semi-leptonic Top-pair Decays Close to Production Threshold*, CMS-PAS-TOP-10007, `http://cdsweb.cern.ch/record/1335720/files/TOP-10-007-pas.pdf`.

[7] CDF Collaboration, *A search for resonant production of $t\bar{t}$ pairs in* 4.8 fb^{-1} *of integrated luminosity of $p\bar{p}$ collisions at* $\sqrt{s} = 1.96$ TeV, `arXiv:hep-ex/11075063`.

[8] D0 Collaboration, *Search for ttbar resonances in the lepton plus jets final state in ppbar collisions at $\sqrt{s}$=1.96 TeV*, Phys.Lett.B **668** (2008) 98–104.

[9] ATLAS Collaboration, *The ATLAS Experiment at the Large Hadron Collider*, JINST **3** (2008) S08003.

[10] ATLAS Collaboration, *The ATLAS Simulation Infrastructure*, `arXiv:physics.ins-det/10054568`.

[11] S. Agostinelli et al., *Geant4 - A Simulation Toolkit*, Nucl. Instr. and Meth. **A506** (2003) 250.

[12] J. A. et. al., *MadGraph/MadEvent v4: The New Web Generation*, JHEP **09** (2007) 028.

[13] T. Sjostrand, S. Mrenna, and P. Skands, *PYTHIA 6.4 physics and manual*, JHEP **05** (2006) 026.

[14] S. Frixione and B.R. Webber, *Matching NLO QCD computations and parton shower simulations*, JHEP **0206** (2002) 029.

[15] P. M. Nadolsky et al., *Implications of CTEQ global analysis for collider observables*, Phys. Rev. **D78** (2008) 013004.

[16] G. Corcella et al., *HERWIG 6: An Event generator for hadron emission reactions with interfering gluons (including supersymmetric processes)*, JHEP **0101** (2001) 010.

[17] J. M. Butterworth, J. R. Forshaw, and M. H. Seymour, *Multiparton interactions in photoproduction at HERA*, Z. Phys. **C72** (1996) 637–646.

[18] M. Aliev et al., *HATHOR HAdronic Top and Heavy quarks crOss section calculatoR*, `arXiv:hep-ph/10071327`.

[19] M.L. Mangano et al., *ALPGEN, a generator for hard multiparton processes in hadronic collisions*, JHEP **0307** (2003) 001.

[20] ATLAS Collaboration, *Luminosity Determination in pp Collisions at sqrt(s) = 7 TeV using the ATLAS Detector in 2011*, `https://atlas.web.cern.ch/Atlas/GROUPS/PHYSICS/CONFNOTES/ATLAS-CONF-2011-116`.

[21] ATLAS Collaboration, *Electron and photon reconstruction and identification in ATLAS: expected performance at high energy and results at* $\sqrt{s} = 900$ *GeV*, `https://atlas.web.cern.ch/Atlas/GROUPS/PHYSICS/CONFNOTES/ATLAS-CONF-2010-005`.

[22] M. Cacciari and G. P. Salam Phys. Lett. B **641** (2006) 57, `http://fastjet.fr/`.

[23] ATLAS Collaboration, *Jet energy scale and its systematic uncertainty in proton-proton collisions at sqrt(s)=7 TeV in ATLAS 2010 data*, `https://atlas.web.cern.ch/Atlas/GROUPS/PHYSICS/CONFNOTES/ATLAS-CONF-2011-032`.

[24] ATLAS Collaboration, *Measurement of the top quark pair production cross-section with ATLAS in pp collisions at sqrt(s) = 7 TeV in dilepton final states*, `https://atlas.web.cern.ch/Atlas/GROUPS/PHYSICS/CONFNOTES/ATLAS-CONF-2011-034`.

[25] B.P. Kersevan and E. Richter-Wąs, *The Monte Carlo event generator AcerMC version 2.0 with interfaces to PYTHIA 6.2 and HERWIG 6.5*, (2004) , `arXiv:hep-ph/0405247`.

[26] P. Z. Skands, *Tuning Monte Carlo Generators: The Perugia Tunes*, Phys. Rev. **D82** (2010) 074018.

[27] P. Nason, *A new method for combining NLO QCD with shower Monte Carlo algorithms*, JHEP 11546 (2004) 040.
S. Frixione, P. Nason, and C. Oleari, *Matching NLO QCD computations with Parton Shower simulations: the POWHEG method* , JHEP **11** (2007) 070.
S. Frixione, P. Nason, and G. Ridolfi, *A Positive-Weight Next-to-Leading-Order Monte Carlo for Heavy Flavour Hadroproduction*, JHEP **09** (2007) 126.

[28] P.M. Nadolsky et al., *Implications of CTEQ global analysis for collider observables*, Phys. Rev. D78 (2008) 013004.

[29] A. Martin, W. Stirling, R. Thorne, and G. Watt, *Parton Distributions for the LHC*, Eur. Phys. J. C **63** (2009) 189.

[30] A. Caldwell, D. Kollar, and K. Kröninger, *BAT - The Bayesian Analysis Toolkit*, Computer Physics Communications **180** (2009) 2197.

[31] T. Sjostrand, S. Mrenna, and P. Skands, *PYTHIA 8*, Comput. Phys. Comm. **178** (2008) 852.

[32] S. Ask et. al., *Identifying the colour of TeV-scale resonances,* `arXiv:hep-ph/11082396`.

[33] A. Sherstnev and R. S. Thorne, *Parton Distributions for LO Generators*, Eur. Phys. J. **C55** (2008) 553.

9 Appendix: Extra public plots

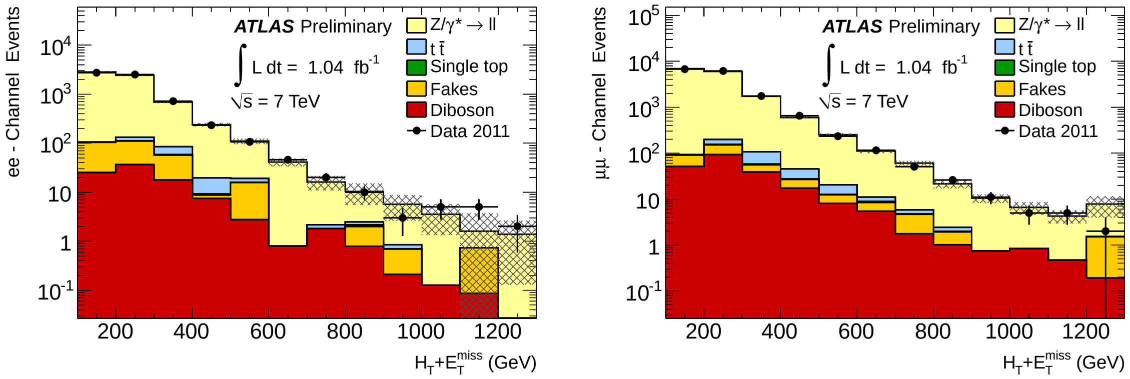

Figure 5: The $H_T + E_T^{miss}$ distributions in the control region. The control region has the Z boson rejection window cut inverted and predominantly selects Z + jets events. The $H_T + E_T^{miss}$ distribution with the Z dielectron (dimuon) mass rejection window cut inverted is shown on the left (right). The points represent ATLAS data and the filled histograms show the simulated backgrounds including the statistical uncertainty represented by the hashed band.

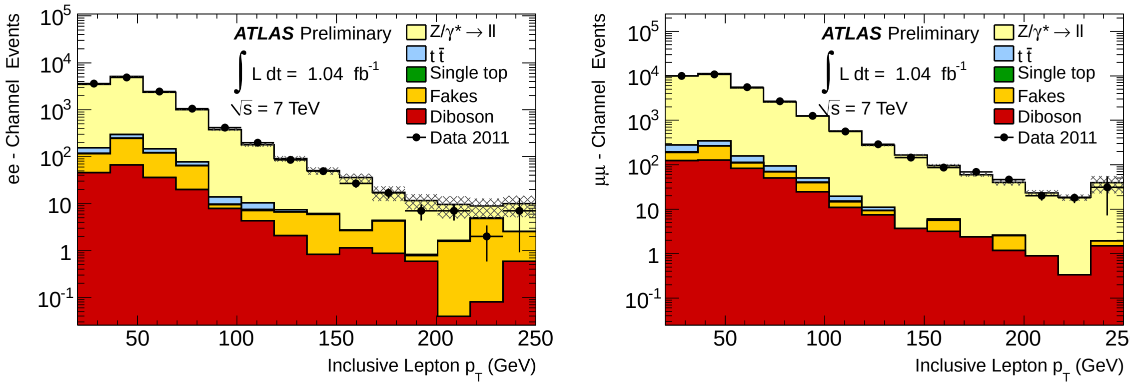

Figure 6: The lepton p_T distributions in the control region. The control region has the Z boson rejection window cut inverted and predominantly selects Z + jets events. The electron (muon) p_T distribution with the Z dielectron (dimuon) mass rejection window cut inverted is shown on the left (right). The points represent ATLAS data and the filled histograms show the simulated backgrounds including the statistical uncertainty represented by the hashed band.

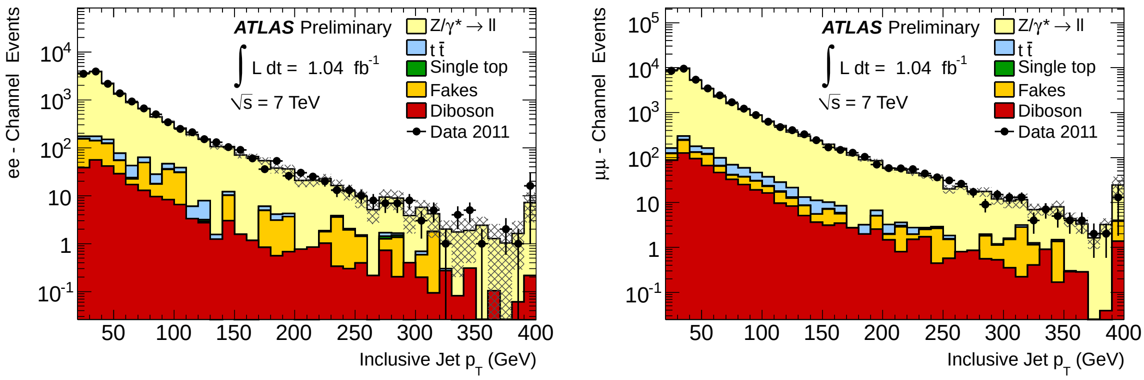

Figure 7: The jet p_T distributions in the control region. The control region has the Z boson rejection window cut inverted and predominantly selects Z + jets events. The jet p_T distribution with the Z dielectron (dimuon) mass rejection window cut inverted is shown on the left (right). The points represent ATLAS data and the filled histograms show the simulated backgrounds including the statistical uncertainty represented by the hashed band.

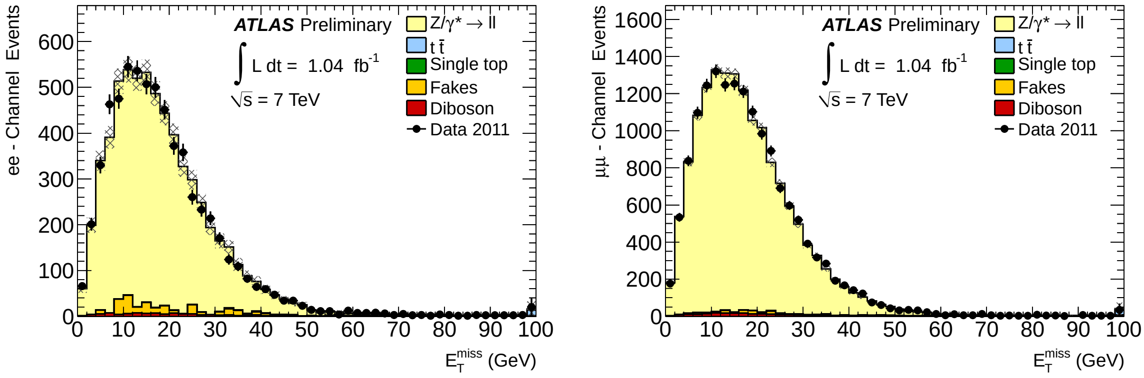

Figure 8: The E_T^{miss} distributions in the control region. The control region has the Z boson rejection window cut inverted and predominantly selects Z + jets events. The E_T^{miss} distribution with the Z dielectron (dimuon) mass rejection window cut inverted is shown on the left (right). The points represent ATLAS data and the filled histograms show the simulated backgrounds including the statistical uncertainty represented by the hashed band.

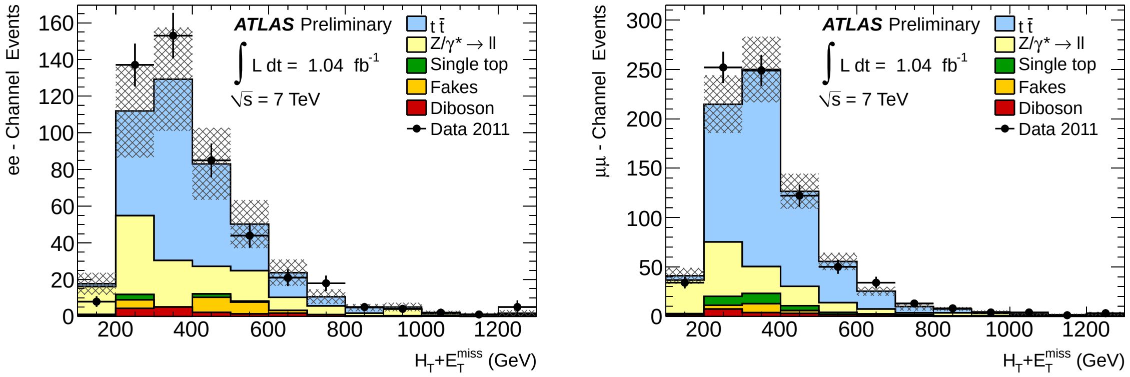

Figure 9: The $H_T + E_T^{miss}$ distribution for dielectron (dimuon) candidate events is shown on the left (right) after all cuts. The points represent ATLAS data and the filled histograms show the simulated backgrounds including the statistical and systematic uncertainty represented by the hashed band.

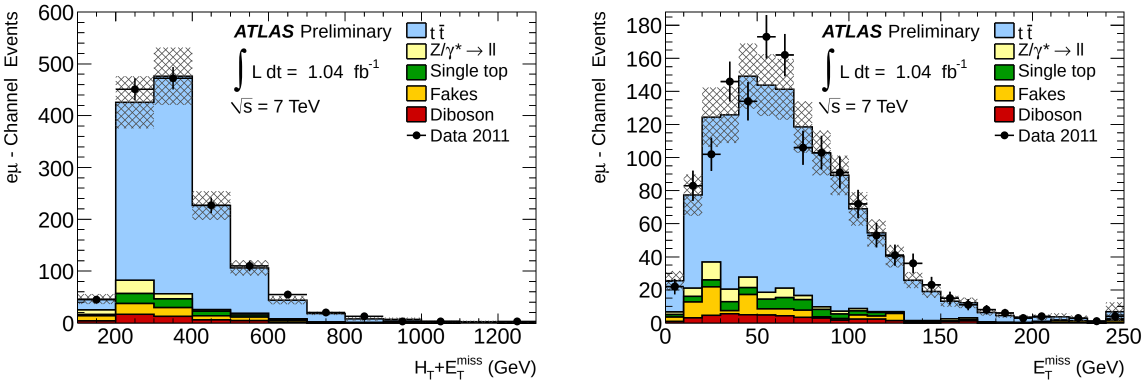

Figure 10: The $H_T + E_T^{miss}$ (E_T^{miss}) distribution for electron-muon candidate events is shown on the left (right) after all cuts. The points represent ATLAS data and the filled histograms show the simulated backgrounds including the statistical and systematic uncertainty represented by the hashed band.

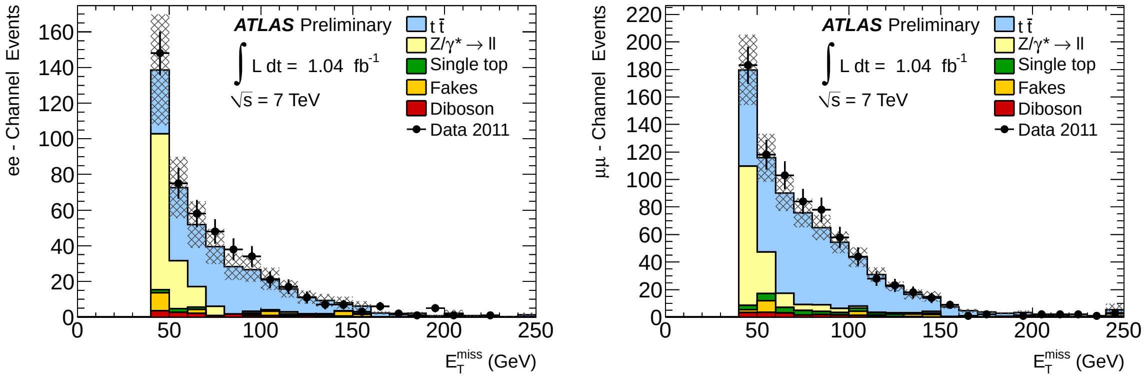

Figure 11: The E_T^{miss} distribution for dielectron (dimuon) candidate events is shown on the left (right) after all cuts. The points represent ATLAS data and the filled histograms show the simulated backgrounds including the statistical and systematic uncertainty represented by the hashed band.

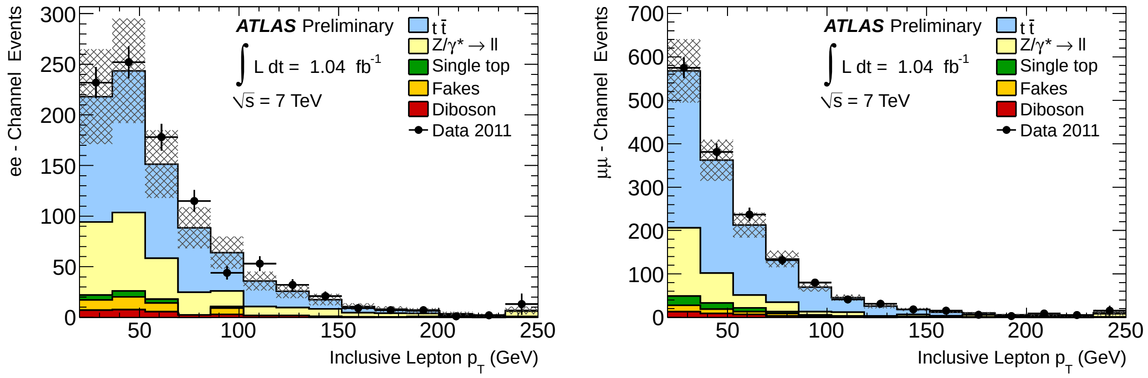

Figure 12: The electron (muon) p_T distribution for dielectron (dimuon) candidate events is shown on the left (right) after all cuts. The points represent ATLAS data and the filled histograms show the simulated backgrounds including the statistical and systematic uncertainty represented by the hashed band.

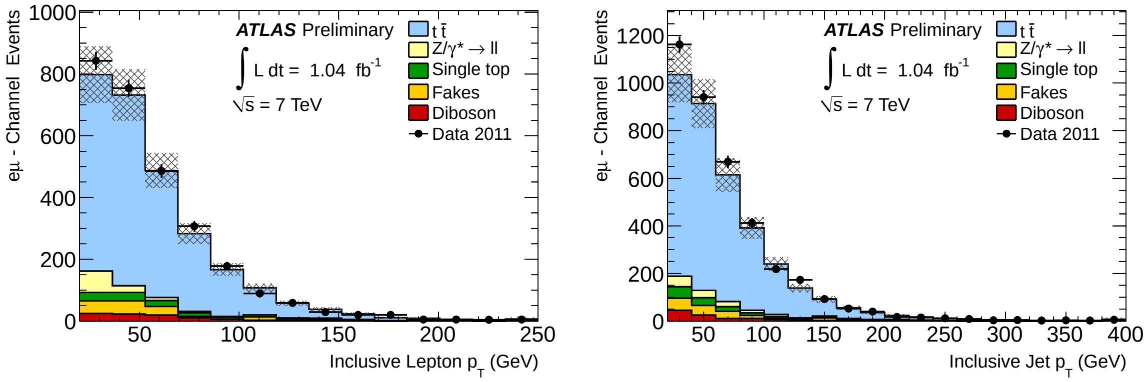

Figure 13: The lepton (jet) p_T distribution for electron-muon candidate events is shown on the left (right) after all cuts. The points represent ATLAS data and the filled histograms show the simulated backgrounds including the statistical and systematic uncertainty represented by the hashed band.

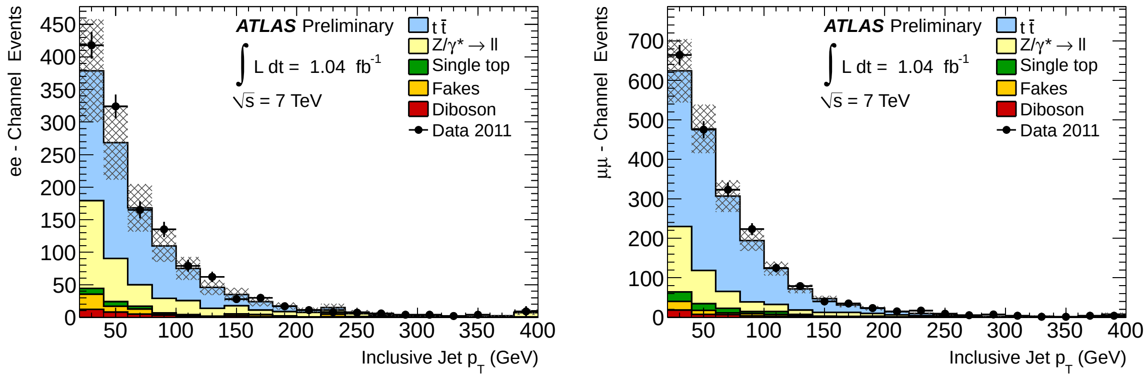

Figure 14: The jet p_T distribution for dielectron (dimuon) candidate events is shown on the left (right) after all cuts. The points represent ATLAS data and the filled histograms show the simulated backgrounds including the statistical and systematic uncertainty represented by the hashed band.

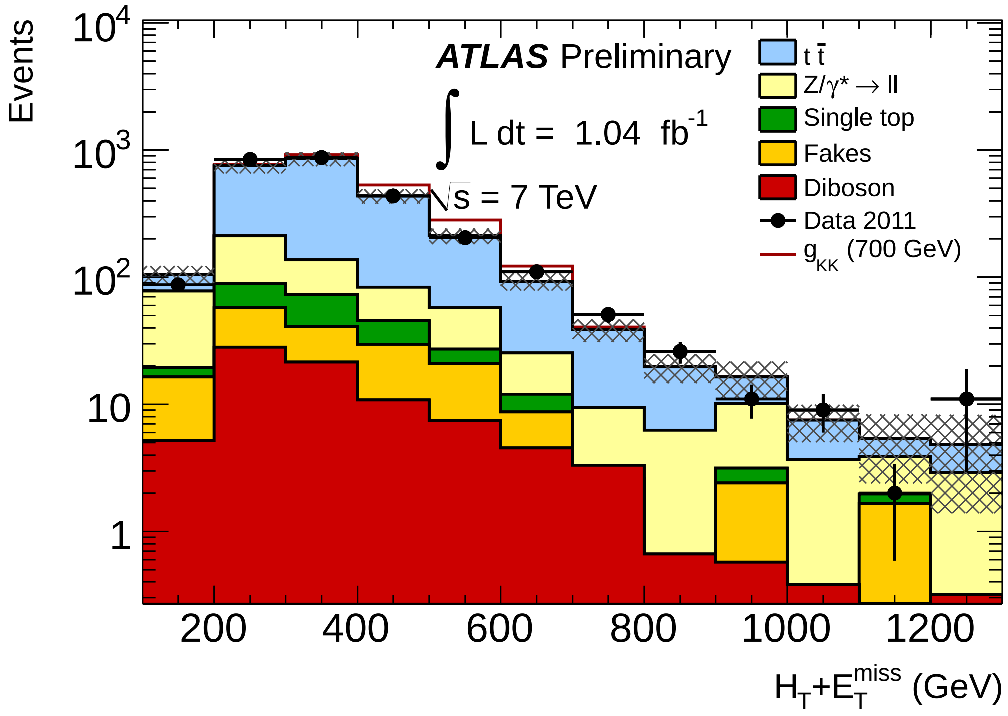

Figure 15: Data - Monte Carlo comparison for the $H_T + E_T^{miss}$ distribution together with a KK-gluon signal with a mass of 700 GeV for illustration. The statistical and systematic uncertainty on the Monte Carlo is represented by the hashed band.

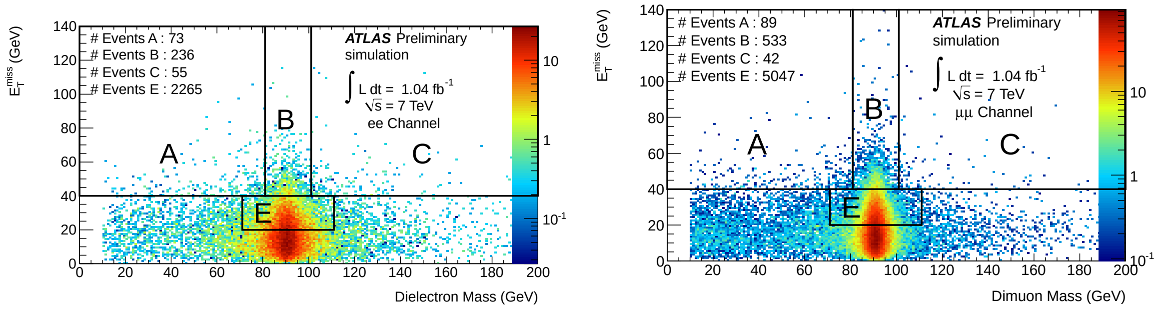

Figure 16: The dielectron (dimuon) mass versus E_T^{miss} distribution for Z + jets Monte Carlo is shown on the left (right). The two distributions are used to normalize the Z + jets background using data. Regions A and C correspond to the signal region, whereas B and E to the control region used in the calculation of the normalization.

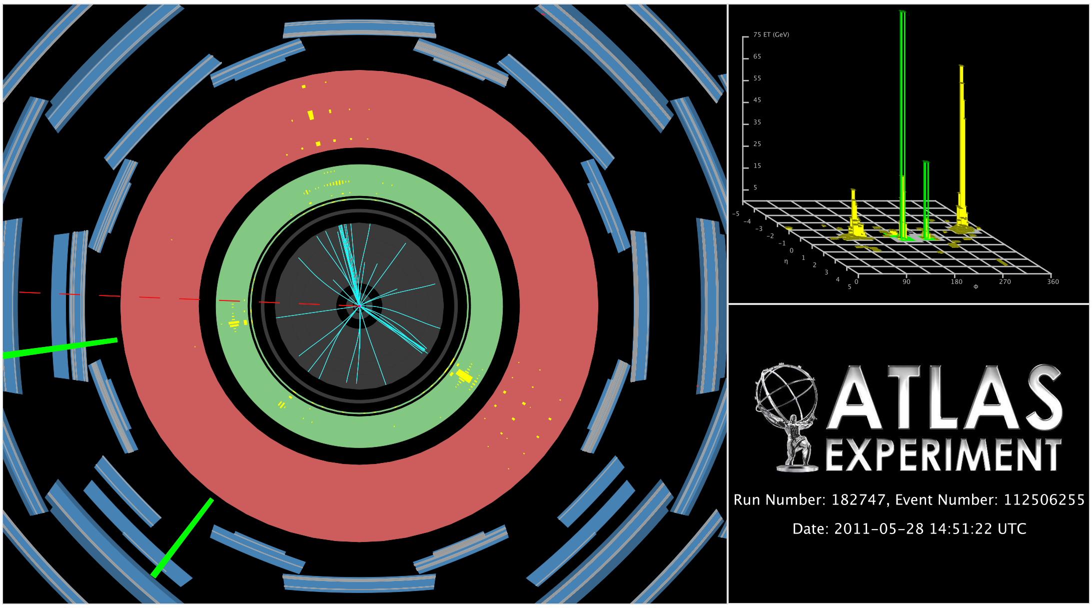

Figure 17: Event display of an event with high $H_T + E_T^{miss}$. The highest energy electron has an E_T of 104 GeV, the subleading electron an E_T of 35 GeV. The highest energy jet has an E_T of 526 GeV, the subleading jet an E_T of 339 GeV. The $H_T + E_T^{miss}$ is 1226 GeV of which 222 GeV originates from E_T^{miss}.